High resolution atlasing of the venous brain vasculature from 7T quantitative susceptibility

Julia Huck, Yvonne Wanner, Audrey P. Fan, Anna-Thekla Schmidt, Sophia Grahl, Uta Schneider, Arno Villringer, Christopher J. Steele, Christine L. Tardif, Pierre-Louis Bazin, Claudine J. Gauthier

Abstract

The vascular organization of the human brain has many consequences for neurological and neurophysiological function, yet it has thus far not been systematically mapped. In this work, the first atlas of the venous vasculature using quantitative susceptibility maps (QSM) acquired at 7T with a 0.6 mm isotropic resolution is presented. The VENAT (Venous Neuroanatomy) atlas was created from 5 separate measurements of 20 young and healthy volunteers using a two-step registration method based on 3D segmentations of the venous vasculature. This cerebral vein atlas includes the average vessel location and diameter from all participants and provides a first measure in vivo of the angio-architectonic organization of the human brain and its variability. This atlas can be used as a basis to understand changes in the vasculature during aging and diseases, as well as vascular and physiological effects in neuroimaging.

Keywords: venous vasculature, QSM, UHF-MRI, vein atlas, vein segmentation, cerebral vasculature

Introduction

Cerebral arteries are known to be affected in aging and diseases such as atherosclerosis and dementia (Peters 2006; Brown and Thore 2011). In part because of this, arteries have long been the main focus of research on the cerebral vasculature. The venous vasculature has been largely ignored, but there is an increasing recognition that valuable information about cerebral physiology, diseases and our measures of brain function could be gleaned from a more thorough understanding of veins.

Veins have received increased attention over the past decades as they are the main sources of contrast in the blood oxygenation level dependent (BOLD) functional magnetic resonance imaging (fMRI) technique (Seiyama et al. 2004; Gagnon et al. 2015). But while different aspects of venous physiology have been explored in the context of the BOLD signal, venous structure has only received a limited amount of attention (Turner 2002; Gagnon et al. 2015). One of the issues of concern is that the BOLD contrast is known to be sensitive to draining veins, which introduce a bias in the measured location of brain activation (Turner 2002). This is because the BOLD signal is based on local changes in the ratio between deoxyhemoglobin (dHb) and oxyhemoglobin due to the hemodynamic response that accompanies changes in neural activity (Logothetis and Wandell 2004). While the BOLD signal is thought to arise partly from the parenchymal response, it has been shown to also have a significant intravascular component, especially at the lower field strengths of 1.5 or 3 Tesla (T) used in most functional studies. This intravascular component has been estimated to be between 40-70% at 3T (Boxerman et al. 1995; Donahue et al. 2011). This is problematic since it is estimated that a vein with a diameter of 0.6mm is able to drain 125mm² of cortex (Turner 2002). This influence of draining veins generates uncertainty in the exact location of brain activity as measured by the BOLD response, but also biases the amplitude of the response measured as draining veins contain more dHb and may therefore contribute the voxels with the highest signal change amplitude. These may then be detected as the most significant areas of signal change. Furthermore, there are indications that vessel orientation may also have a differential impact on the BOLD signal (Gagnon et al. 2015). There are currently no ideal ways of identifying these voxels with large veins in

vivo. However, a venous atlas could in the future be used as a prior to identify the voxels most likely to have a large venous bias in functional MRI studies, and would allow the measurement of orientation-related biases.

It is also increasingly recognized that factors such as aging, injury, diseases such as stroke and dementia, lifestyle changes and physiological training can have a profound impact on brain vascular structure and oxidative metabolism (Kramer et al. 2006; Pathak et al. 2011; Voss et al. 2011). Structural changes in the cerebral vasculature have been shown to occur in post-mortem studies of aging, Alzheimer's disease (AD) and leukoaraiosis (LA) (Brown and Thore 2011). In aging, a reduced vascular density and increased tortuosity has been observed, and these changes are thought to underlie the development of the ubiquitous white matter lesions (WML) (Peters 2006). While these changes have predominantly been studied in terms of the arterial vasculature, Brown et al. report an increased wall thickness in veins and venules of the periventricular white matter with normal aging and a greater degree of wall thickening in patients with LA (Brown and Thore 2011). Furthermore, an increased tortuosity has been associated with LA (Wahlund et al. 2001) and has been shown to be detectable using susceptibility-weighted imaging at 7T (Shaaban et al. 2017). The small size of the veins affected by most of these changes poses a challenge for in vivo imaging however, especially at the field strengths typically used for MRI studies of aging and disease. An atlas of the venous vasculature could help solve some of these issues by providing a strong prior for venous segmentation of susceptibility images and normative information against which to compare aging and disease-related changes.

Magnetic susceptibility is a property of tissues which is dependent on the presence of atoms with magnetic properties such as iron. This property can be imaged using the Quantitative Susceptibility Mapping (QSM) technique, which has been shown to be primarily sensitive to myelin, iron deposition and deoxyhemoglobin in the brain (FAN, etc) (Langkammer et al. 2012; Stüber et al. 2014; Wang and Liu 2015). QSM can be used to image veins, since the presence of paramagnetic deoxyhemoglobin (dHb) molecules creates a difference in magnetic susceptibility in venous blood relative to surrounding tissue. Furthermore, the signal intensity in each venous voxel is directly related to Oxygen Extraction Fraction (OEF) and the cerebral metabolic rate of O2 (CMRO2) through Fick's principle (Fan et al. 2014; Serres et al. 2015). Therefore, QSM is a powerful technique for studying the venous network as it not only provides information about venous structure, but also about local metabolism.

Recognition of the importance of the venous network and the current lack of information about the human venous vasculature, combined with recent developments in susceptibility imaging has already led to the creation of two probabilistic venous atlases. These efforts have focused on generating statistical maps with a high likelihood for a vessel's location, rather than building explicit vascular maps (Ward et al. 2018; Bernier et al. 2018). QSM can however provide more granular and additional information about venous properties, which we seek to leverage here. Knowledge about the most probable location of each vessel, but also vessel diameter and tortuosity would allow a more informed calculation of biases in the BOLD signal and a better understanding of aging and disease-related changes. In this paper we introduce the VENAT (Venous Neuroanatomy) atlas. The atlas is open source atlas and available on figshare (https://figshare.com/articles/VENAT_Probability_map_nii_gz/7205960). This atlas was built using an optimized approach through registration of vascular segmentations and using five images per participant. The VENAT atlas includes a partial volume (PV) map, which shows vessel location, and maps of the diameter, curvature and torsion of vessels.

Methods

Participants

MRI acquisitions were performed in twenty young participants between the ages of 22 and 30 years (average ± SD of 25.05 ± 2.48 years, 10 females) as part of a plasticity study. Identical acquisitions were performed 5 times

over a period of 3 weeks on each participant. All participants were right-handed. None of the participants had a history of neurological disorders or currently suffered from psychiatric disorders as indicated by self-report and a structured clinical interview. The study was approved by the Ethics Committee of the University of Leipzig and was conducted in accordance with the Declaration of Helsinki. All participants gave written informed consent prior to the beginning of the study.

Scan Parameters

Acquisitions were completed on a 7T Siemens Magnetom MR system (Siemens Healthcare, Erlangen, Germany) with a 32 channel Nova head coil (NOVA Medical Inc., Wilmington MA, USA). Two sequences were acquired to generate the vascular atlas: a multi-echo 3D FLASH (Haase et al. 1986) with two echo times (TE) and a whole brain T1 map using the MP2RAGE technique (Marques et al. 2010). Auto-align was used at each session to ensure a comparable placement of the image acquisition between time points. Additionally, dielectric pads were placed the sides of their head to enhance signal in the temporal lobes and the cerebellum (O'Reilly et al. 2016).
The multi-echo 3D gradient echo FLASH image was acquired with a 0.6mm isotropic resolution; flow compensation along all three axes for the first echo; repetition time (TR)= 29 ms; TE = 8.16 ms / 18.35 ms; matrix = 320x320x104; GRAPPA acceleration=3; and bandwidth = 250 Hz/Px. Non-recombined phase and magnitude information was saved.
The whole brain MP2RAGE was acquired with a 0.7mm isotropic resolution and the following parameters: TR=5000ms; TE=2.45ms; matrix=; TI 1 /2= 900 / 2750 ms; Flip angle 1/2 = 5°/3° deg; and bandwidth = 250 Hz/Px. The resulting estimated quantitative T1 (qT1) was used for registration.
Additionally GRE phase reference images were acquired to estimate phase offsets between receive channels for optimal phase combination. The scan parameters were TR = 18ms, TE = 4.08 ms / 9.18 ms, matrix = 128x128x80, flip angle = 10° deg, 2 mm isotropic resolution, and bandwidth = 300 Hz/Px.

Registration to standard stereotactic MNI space

Processing was done using MIPAV 7.4.0 [http://mipav.cit.nih.gov/] and the CBS High-Res Brain Processing Tools for MIPAV (CBSTools) [https://www.nitrc.org/projects/cbs-tools/], except when specified. At each time point, a dedicated skull stripping algorithm was applied to the MP2RAGE images (Bazin et al. 2016). The skull stripped images were then registered linearly to the MNI152 0.5 mm template. The second echo image of the FLASH sequence, which provided good anatomical contrast, was registered linearly to the MP2RAGE image from the same time point. The linear registrations were done using FLIRT (Fischer and Modersitzki 2003) with normalized mutual information and 6 Degrees of Freedom (DoF). The deformation field from the registration from the MP2RAGE images to MNI space and from FLASH to MP2RAGE were concatenated and applied on the first echo from the FLASH sequence in native space to transform these images into MNI space.

Quantitative Susceptibility Map reconstruction

The phase images from each channel were recombined offline using the phase estimates from the low-resolution field maps to ensure a high phase image quality for QSM reconstruction. The combined magnitude (Fig. 1B) and phase (Fig. 1A) of the shorter TE time (TE = 8.16 ms) were used as input for QSM reconstruction. A brain mask was generated by building an average of the MP2RAGE images from all five time points for each participant in MNI space. This average brain mask was generated to ensure a consistent brain size over all time points. The average brain mask was transformed into individual space for each participant and time point by applying the inverse transformation field from the registration of the FLASH images to MNI space.
To brain mask was eroded by 8 voxels to avoid artifacts from the large susceptibility difference at air-tissue interfaces during the QSM reconstruction while preserving as much volume as possible. QSM maps were

created using the Fast L1-Regularized QSM with Magnitude Weighting and SHARP background filtering toolbox (Bilgic et al. 2014) (Fig. 1C) in MATLAB R2016b [The MathWorks, Inc., Natick, Massachusetts, United States]. The toolbox parameters were only modified by changing the field strength parameter from 3T to 7T. In order to use images in the nifti format, a nifti toolbox was included.

Vessel Segmentation

Vessels were segmented using a multiscale vessel filter (Bazin et al. 2016) on the QSM image from each time point. This filter estimates image edges recursively and uses a global probability diffusion scheme to link nearby voxels into vessel branches. It also estimates vessel diameter based on partial volume (PV) of the smaller vessels in a multiscale fashion. Thereby the diameter estimation is able to detect diameters half the voxel size of the resolution using the approximation of woertz (Woerz and Rohr 2004). The filter has been found to be particularly sensitive to small vessels, see (Bazin et al. 2016) for an evaluation. However, due to the high iron content of the smaller basal ganglia nuclei, the vessel filter also detects small basal ganglia nuclei as large vessels. To prevent this erroneous segmentation, the filter was modified here to use the ATAG atlas of 30 young participants as a negative prior (Fig. 1D) (Keuken et al. 2014). For this, the non-linear right and left masks of the striatum, external segment of the globus pallidus, internal segment of the globus pallidus, red nucleus, subthalamic nucleus, substantia nigra, and periaqueductal grey were combined into one mask in MNI space. To transform the ATAG mask from MNI space into individual space, the inverse deformation fields from the FLASH to MNI space registration were applied. To avoid miss-segmentations and segmentation errors due to registration of the QSM images into MNI space, vessel segmentation was done in native space. The segmented vessels were then registered into the MNI152 space by applying the transformation matrices of the FLASH images into the MNI space on the segmented vessels.

Atlas Construction

The atlas was created by registering together the segmented vessels from all images. This type of registration is challenging given the small size of cortical vessels and variability in vessel location. Because of this small size, loss of information can occur if vessels are not aligned at the exact same position, either due to small errors in registration across time points within a participant, to variability in vessel location across participants or due to errors in registration across participants. To prevent this loss of information the segmented vessels in MNI space (Fig. 1E) were reduced to their centerline by applying a skeletonization algorithm adapted from (Bouix et al. 2005) on the probability maps, with a boundary and skeleton threshold of 0.5 (Fig. 1F). These centrelines were then inflated by 15 mm (Fig.1G). This allowed the construction of an average vessel location despite some variability in the precise vessel location.

Diameter maps are an additional output of the vessel filter. These maps depict the diameter in a one voxel thick center line with diameter coded as the intensity value. Additional features like curvature and torsion were calculated from the skeletons of the probability maps in MNI space. The algorithm for calculating the curvature and torsion was adapted from (An et al. 2011).

The transformation maps from the registration were applied on a 2 mm 'inflated diameter, curvature and torsion in order to obtain a proper average even where the alignment was imperfect.

The atlas was built in two steps. First an average across time points for each subject was calculated. These average images were then used as an input for the multi-subject average.

Single Participant Average

The inflated vessels were registered using the SyN module of ANTs (Avants et al. 2009). The reference image used for this registration was the average of the segmented vessels in MNI space (Fig. 1H). The SyN algorithm was run with 40 x 50 x 40 iterations at coarse, medium and fine scales as specified in the CBSTools interface. Registration was done iteratively with each step taking as input the registered image from the previous registration with their resulting average as a reference (Fig. 1G-H).

To follow the improvement from each registration step, the standard deviation of each registered image to the average was calculated. Four registration steps were necessary to bring this average improvement below 10% when building the single participant averages.
For visualization purposes a skeletonization algorithm was then applied on the registered PV maps with the parameters of 0.33 for the boundary and skeleton threshold to return to a one voxel thick map of the diameter, curvature and torsion. The output of the skeletonization was binarized and multiplied with the inflated diameter, curvature and torsion average maps of each participant.

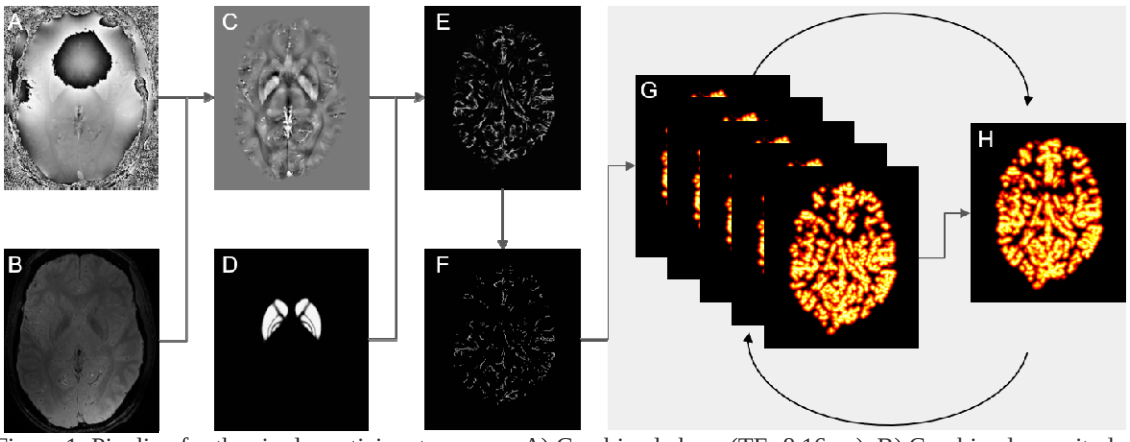

Figure 1: Pipeline for the single participant average; A) Combined phase (TE=8.16ms); B) Combined magnitude (TE=8.16ms); C) QSM; D) ATAG atlas; E) probability map of the vessel segmentation; F) skeletonized vessels; G) skeleton inflated by 15 mm of all time points; H) average of inflated skeletons.

Multi-Participant atlas

The multi-participant atlas was created by using the individual averages as input (Fig. 2A). These single participant averages were combined into a first multi-participant average. However, this first multi-participant average image was blurred due to inter-participant variability (Fig. 2B). To refine the registration, all participants were registered to the participant with the smallest standard deviation from the multi-participant average. For this registration the SyN parameters were again set to 50 x 40 x 50. This registration step was only done once, to ensure a first alignment into the same space and a sharp reference image for the following registration steps (Fig. 2C). After this, multiple iterations using increasingly fine registration parameters were performed to achieve an accurate alignment of the multiple participants. Each registration used the average of the previous registration step as a reference image and the registered images of the previous registration step as input in the SyN algorithm of ANTs. First a coarse registration with SyN was done (40 x 0 x 0) (Fig. 2D). An improvement in standard deviation below 1% was used as convergence criterion for each level of registration (Fig. 3). Thirteen registration steps were required to meet this criterion at the coarse level, followed by seven medium (40 x 50 x 0) (Fig. 2E) and two fine registration steps (40 x 50 x 40) (Fig. 2F).
Similar to the single participant averages a skeletonization algorithm was applied on the final VENAT PV map (Fig. 2G) with the parameter of 0.05 for the boundary and skeleton threshold. The threshold had to be adapted to the values of our new PV map in order to include as much of the smaller vessels as possible. The resulting skeleton was binarized and multiplied with the registered diameter, curvature and torsion maps to return to a one voxel thick maps for the VENAT atlas.

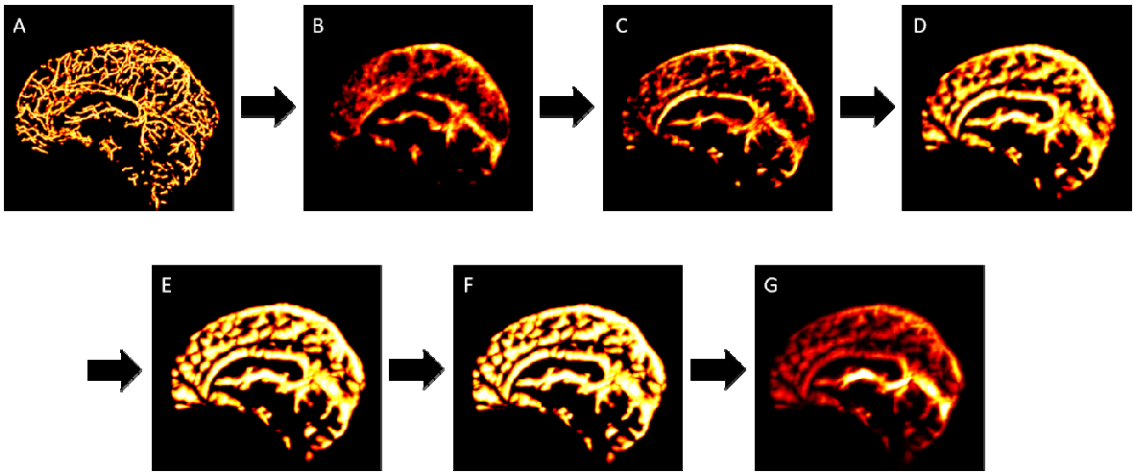

Figure 2: A) Probability map of the participant with the lowest standard deviation; B) First multi participant average of the probability maps; C) Average after registration to the participant closest to the first average; D) Probability average after 13 coarse registrations; E) Probability average after 7 medium registrations; F) Probability average after 2 fine registrations; G) PV map of the VENAT atlas; all maps are maximum intensity projections over 20 slides;

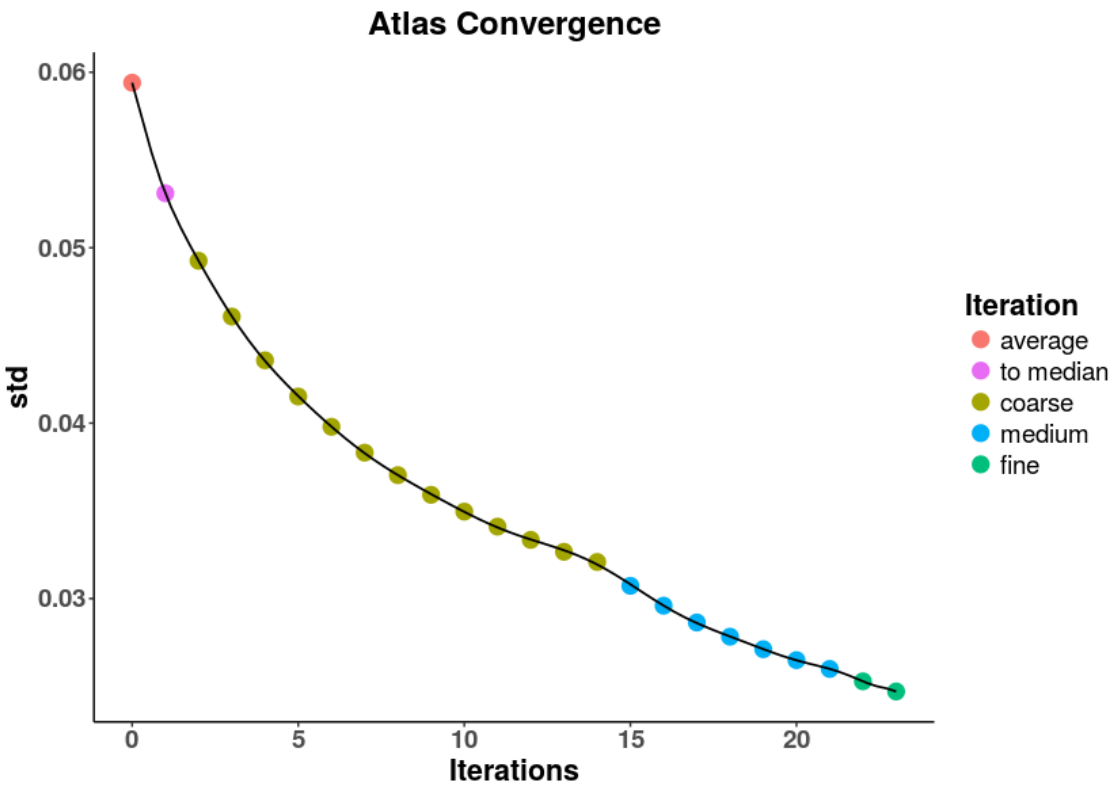

Figure 3: Standard deviation for each iteration step. Average denotes the first average of the single participant averages. To median denotes the registration off all participants to the participant which was closest to the overall average. Iterations were done at each level until the improvement in standard deviation was below 1%.

Results

Single Participant Average

Examples of across-day PV averages are shown in Figure 4 for the participant with the lowest (mean: 0.0149 +- 0.0343) and highest standard deviation (mean: 0.0223 +- 0.0487) across days respectively. The figure shows the PV map across days for two participants and their standard deviation as maximum intensity projections (MIP) in the sagittal, axial and coronal view. In Figure 4, A1 demonstrates data quality for our best participant and shows a high density of vessels over the entire brain. B1 on the other hand shows a lower density of vessels especially in frontal and temporal areas. Furthermore, A1 shows a greater number of smaller cortical veins than B1, which shows mainly larger veins, also appearing blurrier in the image. The standard deviation maps support these observations as A2 shows both lower values across the entire brain than B2, but also a higher consistency in the vessel diameter.

The average diameter across the five time points is given in Figure 5 for the same participants as in Figure 4. Participant A had more vessels with smaller diameters (mean: 0.67+-0.33mm) compared to participant B (mean: 1.01+-0.53 mm). The standard deviation (not shown) was in average 0.071 +- 0.065 for participant A and in average 0.165 +- 0.138 mm for participant B. While most large vessels are not present in the images due to erosion of the mask during QSM reconstruction, part of the sagittal sinus, straight sinus and transverse sinuses are visible in the images, but most visible vessels are smaller cortical vessels. Participant A shows a higher vessel density than participant B, especially in the frontal lobe. Furthermore, participant A shows a lower variability of vessel diameter, especially for the larger vessels, than participant B.

Figure 5 also shows the curvature (A2 and B2) and torsion (A3 and B3) for the participants of Figures 4 . Curvature values were similar for both participants with an average of 0.0918+-0.0438 mm^{-1} for participant A and 0.0906 +- 0.0414 mm^{-1} for participant B. Participant A was found to exhibit a higher torsion (mean: 0.006 +- 0.0054 mm^{-1}) than Participant B (mean: 0.0036 +- 0.0036 mm^{-1}). To evaluate the consistency across the five time points, the standard deviation was calculated for each participant: respectively 0.0618 +- 0.0276mm^{-1} for Participant A and 0.072 +- 0.0252mm^{-1} for Participant B for curvature, and 0.006 +- 0.0042 mm^{-1} for Participant A and 0.00462 +- 0.0042 mm^{-1} for participant B. More generally, the curvature was found to be more stable across participants and to be relatively robust to differences in data quality, while the torsion was found to vary more across participants.

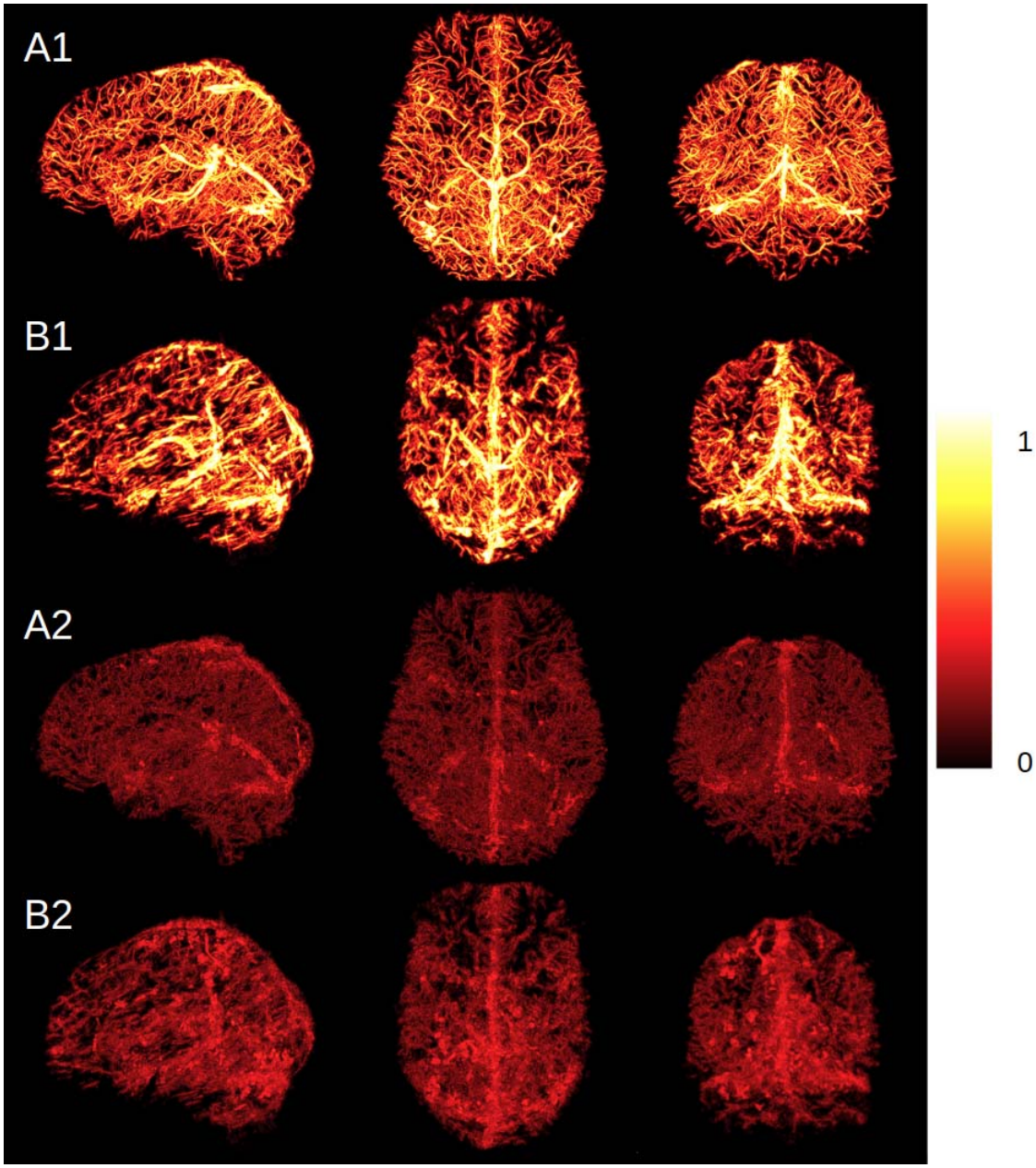

Figure 4: Maximum intensity projection over all slides of 1) the PV maps and 2) the standard deviation; A) participant with the highest standard deviation; B) participant with the lowest standard deviation; both participants are depicted in the sagittal, axial and coronal view.

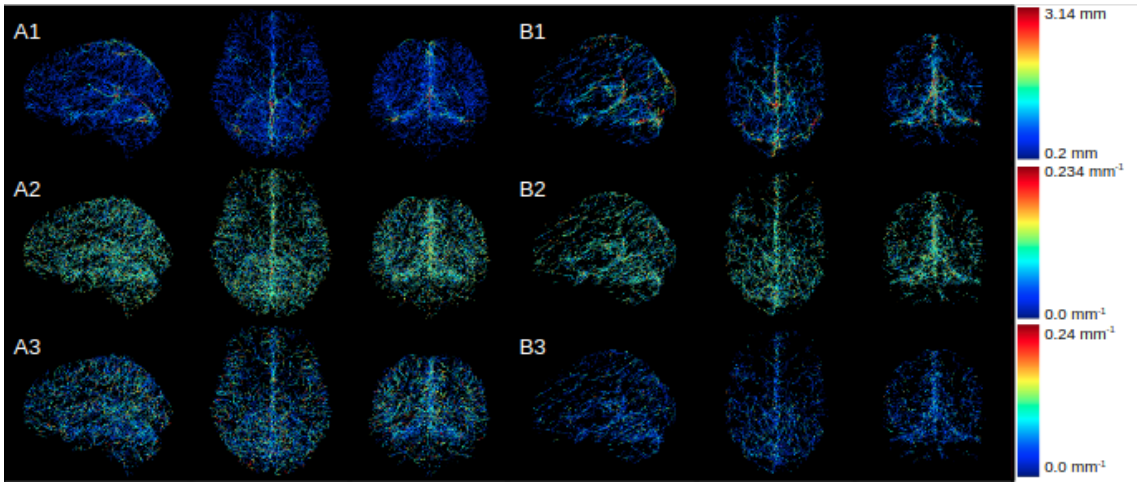

Figure 5: Maximum intensity projection over all slides of the diameter maps (1) , curvature (2), and torsion (3); A) participant with the highest standard deviation; B) participant with the lowest standard deviation; both participants are depicted in the sagittal, axial and coronal view.

Multi-participant average

Figure 6, 7 and 8 present the PV map of the VENAT atlas. Figure 6 displays a MIP over all slices and the corresponding standard deviation map of the 20 participants. Figure 7 and 8 show the same PV map with a MIP over 20 slices in the axial view from inferior to superior and in the sagittal view from right to left, to better appreciate the distribution of vessels over the brain. The intensities of the PV range from 0 to 0.8. The distribution of vessels was found to differ across brain regions and to be highest in the occipital lobes and the cerebellum. These regions also show a higher variability compared to other brain regions. The frontal lobe, except for the longitudinal fissure, is more sparsely distributed than the other brain areas.

Figure 9 shows the average diameter (A), curvature (B) and torsion (C) maps of the VENAT atlas in the sagittal, axial and coronal view. The average diameter maps are in the same range as individuals (mean: 0.84 +- 0.33 mm) but with increased standard deviation (mean: 0.26 +- 0.15 mm) reflecting inter-participant variability. Like the diameter values, average curvature and torsion are comparable in the VENAT atlas and single participant averages: 0.107 +- 0.013 mm^{-1} for curvature and 0.004 +- 0.0012 mm^{-1} for torsion. Standard deviation maps across all participants were similar to individual participants values (curvature: 0.059 +- 0.011 mm^{-1}, torsion: 0.003 +- 0.0012 mm^{-1}).

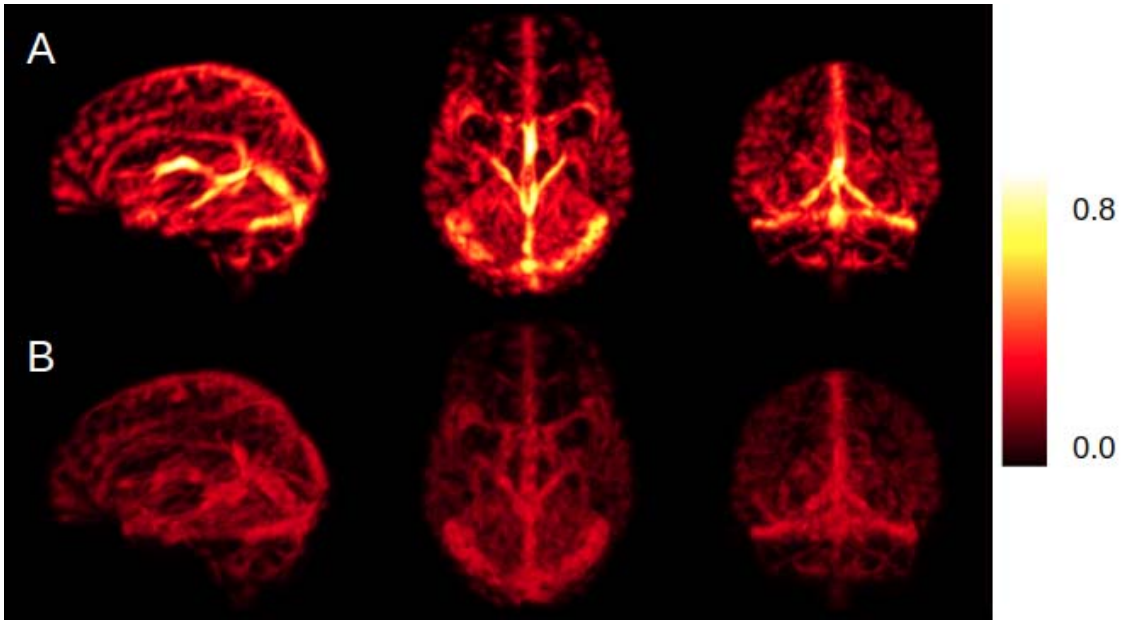

Figure 6: Maximum intensity projection over all slides of the PV map (A) and the standard deviation (B); the VENAT PV atlas is depicted in the sagittal, axial and coronal view

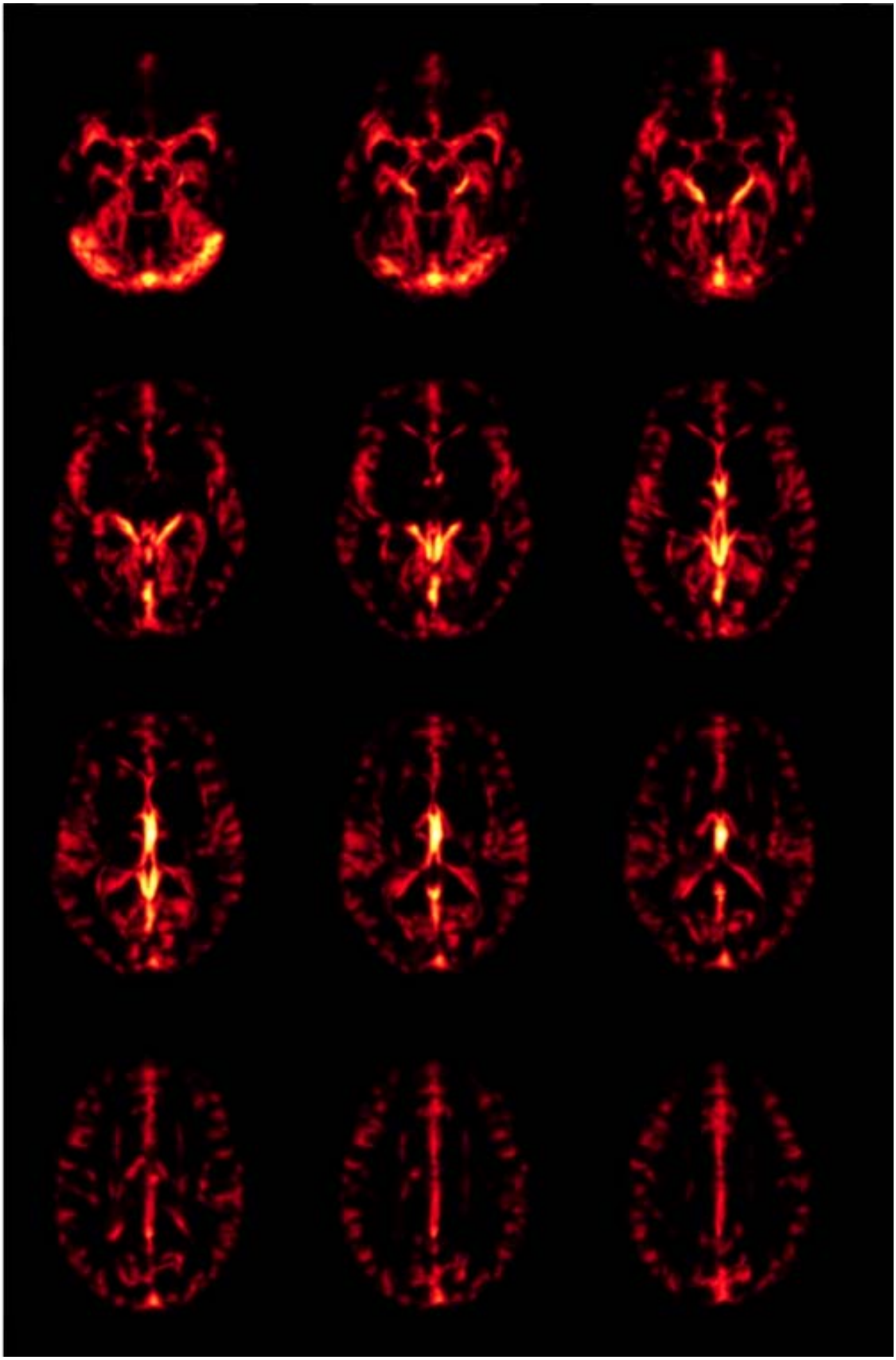

Figure 7: Maximum intensity projection over 20 slides; the images are depicting the partial volume map of the atlas from inferior to superior

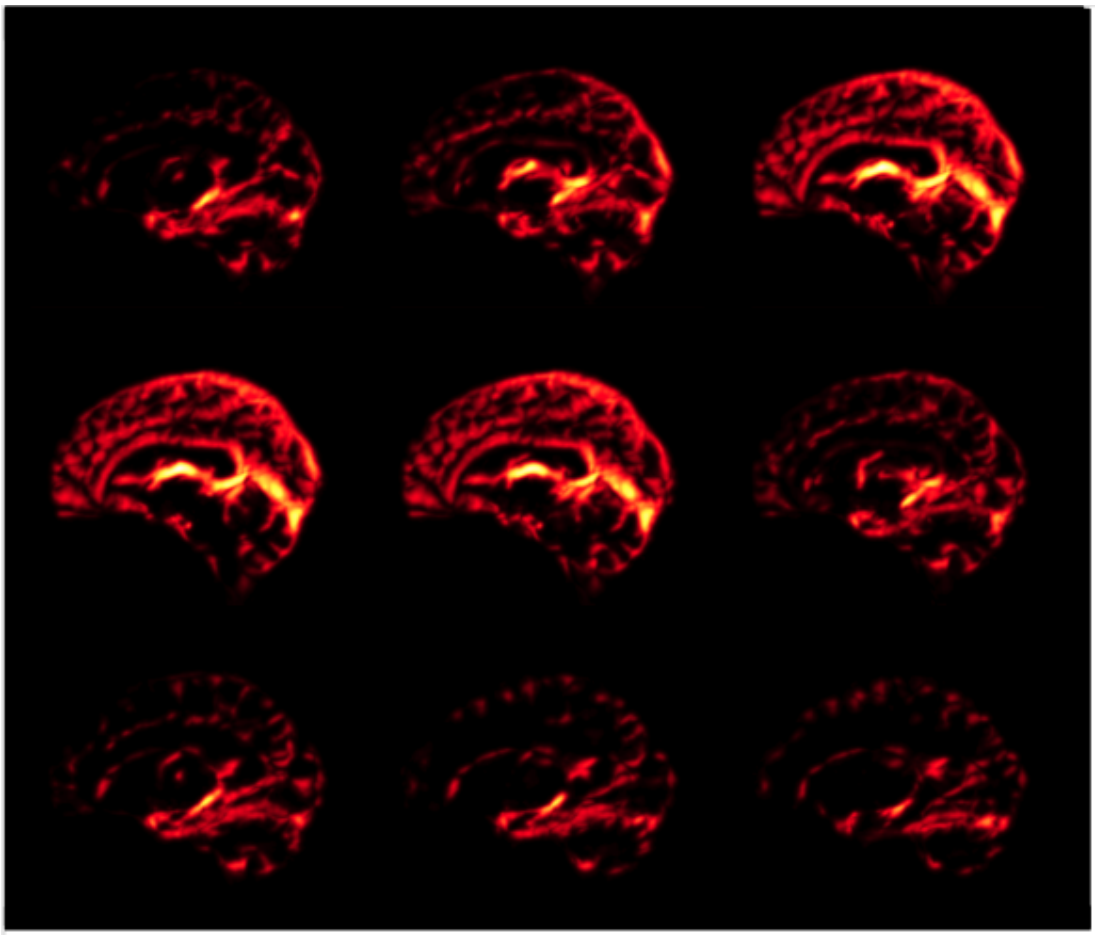

Figure 8: Maximum intensity projection over 20 slides; he images are depicting the partial volume map of the atlas from right to left

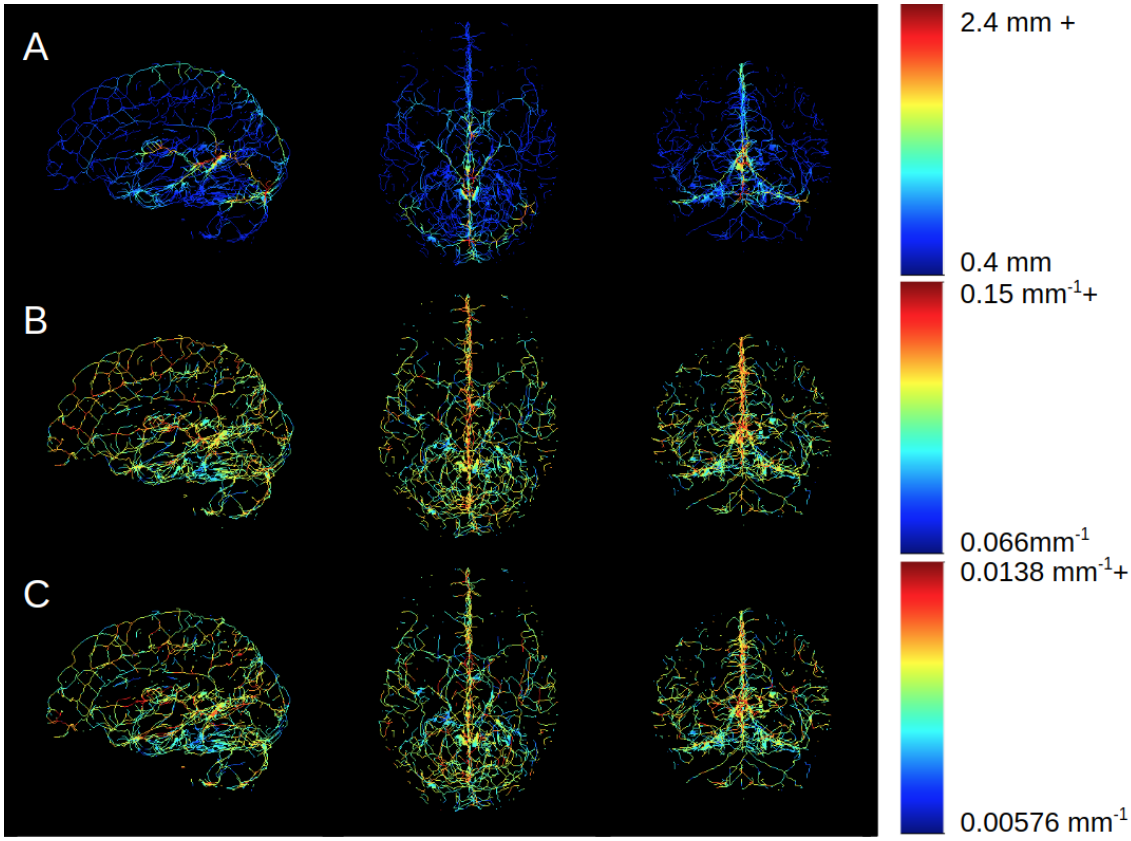

Figure 9: Average vessel diameter (A), curvature (B) and torsion (C) of the atlas.

Discussion

Summary of Results

Here we present a high resolution atlas of the cerebral venous vasculature based on 7T QSM in 20 young people with five acquisitions each. This atlas was generated through multi-step registration of segmented vessels and therefore shows the average venous positions across participants. The inclusion of multiple QSM maps for each participant ensured a high-quality input vessel map for each participant for the subsequent across-participant registration. The atlas shows that vessels are consistent across time points within a single individual, leading to high quality individual vessel maps across days with low standard deviations. The multi-participant atlas highlights the high variability in vessel location, but especially in vessel diameter across individuals. The VENAT atlas also includes maps of the curvature and torsion of vessels, providing additional information about venous structure as compared to previous atlases. Overall, the VENAT atlas is the highest resolution venous atlas currently available and, combined with the additional parameters included in the atlas, will be an ideal tool for investigating the venous contribution of BOLD signals, as well as for the study of venous changes in aging and disease.

<u>Single participant average</u>
To improve the quality of the individual inputs into the across-participant registration, we used five QSM acquisitions per participant. This was both to increase signal-to-noise ratio and to reduce spurious vessels due to

noise in our segmentations. Across-day individual averages for the best and the worst participants illustrate the range of data quality used in this atlas. Better participants have a large number of small vessels, a relatively consistent density across the entire brain and low standard deviation. Higher amounts of movement in some participants led to decreased venous contrast and signal-to-noise ratio, making the segmentation less consistent across days, which result in a lower and more locally variable distribution of larger and blurrier vessels.
This impact of data quality is also visible in larger diameter estimates and a larger standard deviation for noisier participants, highlighting the fact that the uncertainty added by lower quality data is expressed more strongly in the diameter estimates than in the position of vessels. This is more likely due to the fact that we inflate the skeleton by 15 mm to do the registration, so that vessels which are not as well segmented across days still become registered together, but there remains more uncertainty on their exact diameter.
Curvature estimates appear largely uninfluenced by data quality differences, at least within the range of this study which included only experienced 7T participants. Torsion on the other hand was found to be lower in participant B, indicating that this metric may be more sensitive to data quality. This might be due to the fact that the calculation of the torsion is using higher order derivatives than the curvature. Therefore, curvature may be a better metric to use when comparing vessel structure across the lifespan or in disease populations, as data acquired in older adults and patients is more likely to be more noisy from a higher iron content (Wayne Martin et al. 1998; Zecca et al. 2004)and a higher degree of movement. Unfortunately, there is to our knowledge no ground truth quantification on the curvature expected from human venous vasculature in vivo. While post-mortem work has shown curvature and torsion to increase with age and diseases (Brown and Thore 2011), the curvature and torsion are typically not quantified per se. The validity of the estimates remains therefore to be established. Nevertheless, the data presented here is a first step toward establishing normative values for QSM-based estimates of curvature and torsion.

Vessel atlas

The individual averages across five days were then used to create the VENAT atlas from 20 participants, thus combining 100 measurements of the vasculature. The resulting atlas shows a prominent contribution of larger veins, indicating a lower variability in position for larger veins. This is consistent with other atlasing work by Bernier et al. and Ward et al. (Ward et al. 2018; Bernier et al. 2018). Smaller veins, while abundant in the individual averages, are sparser in the across-participant average. This is despite the fact that the higher field and resolution used here allowed us to detect smaller cortical veins than in these previous atlases. This highlights one of the difficulties of venous atlasing, since the position and shape of smaller vessels is highly variable across individuals.
Vessel number was found to be less consistent across brain region in the atlas as compared to the single participant averages. The occipital lobe for example shows a higher number of vessels, consistent with previous work (Pfeifer 1927, 1940; Duvernoy et al. 1981; Bernier et al. 2018). The vessels in the frontal lobes are more sparsely distributed than the single participant averages however, probably due to the larger relative number of smaller vessels, which are more variable across participants and therefore underrepresented in the atlas.
The partial volume atlas ranges from 0 to 0.8 (Figure 6), while PV in the individual participant averages include values between 0 and 1 (Figure 4). This further emphasizes the variability across individuals, since this not only indicates that no voxel is entirely venous in the multi-participant average, but also that the variability across participants means that no vessel is ever completely consistent across participants. This is especially striking for larger veins which span more than one voxel, since even though registration of these vessels is somewhat straightforward, there is never any complete agreement on their exact location or diameter. As in the individual participants, the partial volume and diameter standard deviation maps demonstrate a high variability in vessel diameter especially for larger vessels, due both to the segmentation errors mentioned previously, but also to some inter-participant variability in vessel location being translated into diameter variability in the registration step. The atlas also shows fewer vessels of small diameters as these are more variable and may not have been successfully registered across participants. This variability across participants in smaller veins especially is both consistent with other atlases and with existing post-mortem work (Duvernoy et al. 1981; Ward et al. 2018; Bernier et al. 2018).

The curvature and torsion atlas have similar values and variability as the individual participants, largely due to the fact that these measures are extracted on the single participant level and averaged. Compared to vessel diameter, both measures appear more stable across participants. Validation with other techniques, including post-mortem work, would help determine whether the curvature and torsion values of the VENAT atlas correspond to true population averages or whether the measurements are impacted by vessel variability across individuals and represent underestimates of the true curvature and torsion. However, as no quantitative measurement of curvature and torsion in human cerebral veins could be found, no comparison was possible for this work.
Finally, the VENAT atlas includes an orientation map. This map shows good agreement with post-mortem work, with a large proportion of cortical veins being perpendicular to the cortex (Pfeifer 1927, 1940; Duvernoy et al. 1981) and the expected orientation for larger veins.

Other venous atlases

The recent increased interest in venous physiology has led to two other venous atlases being published recently (Ward et al. 2018; Bernier et al. 2018). The first atlas was presented by Ward et al. and is a probabilistic atlas based on combinations of QSM, SWI and manual venous segmentations. This atlas was created through averaging individual venous maps created from an optimized combination of these three types of images, but without explicitly registering the segmented vessels. Rather, matrices from T1 to MNI152 registration were applied to these individual vascular trees. The atlas therefore consists of a venous vessel probability map, rather than a vessel atlas. One advantage of this atlas is the fact that since all three types of images were used, the atlas includes the contribution of large veins which were obtained from SWI and the basal ganglia, which were obtained from manual segmentations. These last two compartments were necessarily excluded from this atlas since iron content causes spurious vessels to be segmented in the basal ganglia in QSM maps and since the erosion of the brain mask required for QSM reconstruction leads to the exclusion of larger sinuses at the surface of the brain. This atlas has however several advantages as it is based on a larger group of participants, and a higher resolution image acquisition at higher field strength, allowing us to detect smaller vessels. Furthermore, by registering vascular trees rather than applying a T1 weighted-based registration on vessel trees, we are able to recover important information about venous structure such as average location, diameter, curvature and torsion. One difference between these two atlases is also the age range included. While the atlas proposed by Ward et al. includes a wide age range (52.6 ± 25.2 years), ours is based only on healthy younger adults (25.1 ± 2.5 years). While this may make the Ward et al. atlas more valid as a lifespan atlas, this new atlas may represent a more normative representation of the vasculature, before any aging or disease-related changes have occurred. Therefore, it could be used to study age and disease-related changes, but should be used with caution when calculating biases in the BOLD signal for example. More studies on vascular changes in aging and disease are required to understand whether any changes can be observed in the range of diameters detectable using this atlas.

The second probabilistic atlas was created by Bernier et al. This atlas differs both from the Ward et al. atlas and the one presented here as it is both an arterial (based on time-of-flight angiography) and venous atlas. The venous portion is based on 3T SWI imaging. Similarly to the VENAT atlas, the atlas presented by Bernier et al. is based on non-linear registration of venous segmentations, also performed using ANTS. The age ranges used for the creation of both atlases are also similar. The VENAT atlas provides some advantages however. The main advantage derives from the higher field and resolution at which it was acquired, allowing us to detect veins as small as 0.3 mm in diameter (Bazin et al. 2016) as opposed to the 0.6 mm limit of the atlas proposed by Bernier et al. Furthermore, the higher field strength provides a higher contrast, which further enhances our ability to detect smaller veins (Duyn et al. 2007). On the other hand, the use of SWI instead of QSM allowed Bernier et al. to map larger veins, since these appear with excellent contrast in SWI maps, but are shaved off at least partially in QSM when eroding the brain mask for reconstruction to avoid artifacts from air-tissue interface. Because of this, the VENAT atlas only contains veins up to 3mm, but the Bernier et al. atlas includes veins up to 5 mm. However, the use of SWI may be suboptimal for detection of veins in the falx cerebri (Ward et al. 2018). Ward et al. showed that QSM can more appropriately detect these veins. Fan et al. (Fan et al. 2014) has shown that

orientation influences SWI image. Furthermore, the inclusion of non-local sources in SWI may lead to overestimation of small vein diameter (Haacke et al. 2004; Ward et al. 2018). This would be problematic for example in calculating bias in BOLD maps as it would lead to an overestimation of the BOLD bias in voxels with small veins.

Other advantages of the VENAT atlas include the multiple time points used to build the individual segmentations used as input into the atlas. This resulted in a higher data quality for these individual inputs and lessened the need for denoising algorithms such as non-local means filter used by Bernier et al. This also ensured that the vessels included in the individual inputs were real vessels, reproducibly detected across days. The VENAT atlas also included additional registration steps as compared to the atlas presented by Bernier et al, resulting in a lower standard deviation across participants in the final atlas. This lower standard deviation results in a better defined atlas with less blurriness.

The general features of both atlases are similar, with the location of larger veins being the most stable, though a higher variability in diameter in these veins was observed here. This may be due in part to the masking operation, leading to a varying degree of masking of the surface veins across participants, but larger veins not close to the brain boundary also show this higher variability. As the standard deviation across participants is not shown in Bernier et al. however, it is not possible to assess whether this variability in diameter is also present when using SWI.

Implications of our work

Venous atlases are a recent development, both for technical reasons and because the importance of venous physiology is increasingly recognized. One of the most obvious areas of application for these venous atlases is for calculating bias in BOLD-based imaging. The BOLD signal is venous in nature and since the highest signal is where there is most deoxyhemoglobin, larger veins can contribute significantly. It has been estimated that the intravenous contribution to the BOLD signal at 3T is 40-70%, but in addition to this, highly stringent thresholding of statistical maps may further enhance this effect by selecting only the most prominent, and therefore venous voxels. This is problematic both in terms of interpretation of the magnitude of the effect, but also in localizing the effect as draining veins even as small as 0.5 mm can be around 10 mm away from the parenchymal area it drains (Turner 2002). Estimates based on this analysis by Turner of the Duvernoy atlas would indicate that the parenchyma drained by the smaller veins visible in our atlas (0.6 mm) can be up to 15 mm away from the location of the veins. While techniques exist, such as spin echo BOLD fMRI, to minimize the intravascular venous contribution, these techniques suffer from a lower sensitivity than gradient echo fMRI (Parkes et al. 2005). An alternative approach would be to try to estimate this bias. The three atlases presented so far (Ward, Bernier, us) could all be used as priors in fMRI analysis to reduce or at least understand the impact of large veins on activation detection using fMRI. The advantages of our atlas however are both related to its higher resolution, allowing the detection of bias from smaller draining veins, and to the additional metrics it includes. Venous diameter could be used to estimate the relative bias of differently sized veins, while curvature maps could help detect bias due to orientation as compared to the main magnetic field. Recent work by Gagnon et al. has suggested that orientation of the cortex in a given voxel may have an impact on the BOLD signal (Gagnon et al. 2015). This is likely to also apply to signal arising from draining veins and detected as areas of high activity in fMRI analyses. This type of orientation-related bias from draining veins could be estimated using curvature maps from our atlas.

The other application of this work is in helping us understand aging and disease-related changes in brain physiology. This could both be in understanding the changes in aging and disease-related biases in the BOLD signal, but also in comparing venous or OEF maps to our normative population. Aging, vascular diseases and dementia are associated with changes to the venous vasculature such as venous collagenosis (Brown et al. 2002) and changes in vessel tortuosity (Wahlund et al. 2001). These will affect venous diameter and curvature. While these changes have never been quantified in vivo, atlases such as the one proposed here could in the future be used as normative data to attempt to detect and quantify these changes in vivo.

Limitations

The main limitation of this work is related to resolution as only larger veins (> 0.2mm) can be measured. This is problematic as much of the bias in BOLD arises from smaller veins and much of the changes in aging and disease also occurs in smaller veins (Brown and Thore 2011). This limited resolution is a consequence of limited acquisition time in live participants, as well as time limitations due to the impact of movement on QSM data quality. This limited resolution also makes validation of this work more difficult as published post-mortem work such as the Duvernoy atlas (Duvernoy et al. 1981) only includes veins up to 380 um. However, the higher field strength used for this atlas allowed the use of a higher resolution than for previous atlases. Future work using prospective motion correction and other advanced acquisition schemes may provide even higher resolutions for vascular atlasing.

Vessel segmentation based on QSM is also challenging for the largest veins and sinuses located at the surface of the brain, due to the masking required for the QSM reconstruction to avoid streaking artifacts from air-tissue interface. In this work, an erosion of 8 voxels was required to avoid these artifacts. As a result of this, the largest veins such as the sagittal sinus were not entirely depicted in the QSM images, leading to a larger variability in the detected diameter of the larger veins close to the cortex across participants. We hope to remedy this problem by combining SWI images and QSM for the segmentation of the larger veins at the surface of the cortex, or by performing a more approximate QSM reconstruction for locating vessels at the surface of the cortex in spite of the artifacts.

An additional aspect is the data quality and the reproducibility of the QSM reconstructions. Though the reproducibility of QSM maps at 3T has been shown to be high (Deh et al. 2015) , the reproducibility of vessel segmentations has never been assessed. Here we show that in high quality data, a consistent dense vessel tree can be reconstructed, but that even small variations in data quality can impair the ability to detect smaller veins or can lead to variations in the diameter estimation. The effect of data quality seems to have also a larger influence on the estimation of the torsion, since the torsion calculation uses high order derivatives. Prospective motion correction of QSM acquisitions could lessen the impact of motion on data quality and render these techniques more robust. Even with highly reproducible vascular trees as in our best participants, the intrinsic variability of human vasculature is a challenge to atlasing. While we could show that careful alignment of the vascular tree across participants provides a detailed map for many veins, it is also clear that measures from individual segmentations are more informative than atlas-based trends, for instance when assessing biases in BOLD responses.

Conclusion

The VENAT atlas is the first atlas depicting veins using an ultra-high field MRI at 7 Tesla. It was built by using a multi-step registration on segmented veins. An average image of each participant across multiple time points was used as an input for the atlas itself. The atlas consists out of 4 maps: partial volume, diameter, curvature, and torsion, which are all freely available (https://figshare.com/articles/VENAT_Probability_map_nii_gz/7205960). We hope that this VENAT atlas can be used in clinical and research studies to better understand the influence of aging and diseases on the venous vasculature but also to estimate biases in BOLD measurements due to the variability of the metabolism.

Acknowledgement

The authors thank Domenica Wilfling and Elisabeth Wladimirov for their help with data acquisition and logistics. This work was supported by the Canadian National Sciences and Engineering Research Council (RGPIN-2015-04665), the Heart and Stroke Foundation of Canada (N.I.A. C.J.G.), the National Institute of Health (1K99NS102884) and the Quebec Bio-Imaging Network (QBIN) for the scholarship for Training course abroad.

References

An Y, Shao C, Wang X, Li Z (2011) Geometric properties estimation from discrete curves using discrete derivatives. Comput Graph 35:916–930. doi: 10.1016/j.cag.2011.02.001

Avants BB, Tustison N, Song G (2009) Advanced Normalization Tools (ANTS). Insight J 2:1–35. doi: http://hdl.handle.net/10380/3113

Bazin P-L, Plessis V, Fan AP, et al (2016) Vessel segmentation from quantitative susceptibility maps for local oxygenation venography. In: 2016 IEEE 13th International Symposium on Biomedical Imaging (ISBI). IEEE, pp 1135–1138

Bernier M, Cunnane SC, Whittingstall K (2018) The morphology of the human cerebrovascular system. Hum Brain Mapp. doi: 10.1002/hbm.24337

Bilgic B, Fan AP, Polimeni JR, et al (2014) Fast quantitative susceptibility mapping with L1-regularization and automatic parameter selection. Magn Reson Med 72:1444–1459. doi: 10.1002/mrm.25029

Bouix S, Siddiqi K, Tannenbaum A (2005) Flux driven automatic centerline extraction. Med Image Anal 9:209–221. doi: 10.1016/j.media.2004.06.026

Boxerman JL, Bandettini PA, Kwong KK, et al (1995) The intravascular contribution to fmri signal change: monte carlo modeling and diffusion weighted studies in vivo. Magn Reson Med 34:4–10. doi: 10.1002/mrm.1910340103

Brown WR, Moody DM, Challa VR, et al (2002) Venous collagenosis and arteriolar tortuosity in leukoaraiosis. J Neurol Sci 203–204:159–163. doi: 10.1016/S0022-510X(02)00283-6

Brown WR, Thore CR (2011) Review: cerebral microvascular pathology in ageing and neurodegeneration. Neuropathol Appl Neurobiol 37:56–74. doi: 10.1111/j.1365-2990.2010.01139.x

Deh K, Nguyen TD, Eskreis-Winkler S, et al (2015) Reproducibility of quantitative susceptibility mapping in the brain at two field strengths from two vendors. J Magn Reson Imaging 42:1592–600. doi: 10.1002/jmri.24943

Donahue MJ, Hoogduin H, van Zijl PCM, et al (2011) Blood oxygenation level-dependent (BOLD) total and extravascular signal changes and $\Delta R2^*$ in human visual cortex at 1.5, 3.0 and 7.0 T. NMR Biomed 24:25–34. doi: 10.1002/nbm.1552

Duvernoy HM, Delon S, Vannson JL (1981) Cortical blood vessels of the human brain. Brain Res Bull 7:519–579. doi: 10.1016/0361-9230(81)90007-1

Duyn JH, van Gelderen P, Li T-Q, et al (2007) High-field MRI of brain cortical substructure based on signal phase. Proc Natl Acad Sci U S A 104:11796–801. doi: 10.1073/pnas.0610821104

Fan AP, Bilgic B, Gagnon L, et al (2014) Quantitative oxygenation venography from MRI phase. Magn Reson Med 72:149–159. doi: 10.1002/mrm.24918

Fischer B, Modersitzki J (2003) FLIRT: A Flexible Image Registration Toolbox. Springer, Berlin, Heidelberg, pp 261–270

Gagnon L, Sakadžić S, Lesage F, et al (2015) Quantifying the Microvascular Origin of BOLD-fMRI from First Principles with Two-Photon Microscopy and an Oxygen-Sensitive Nanoprobe. J Neurosci 35:3663–75. doi: 10.1523/JNEUROSCI.3555-14.2015

Haacke EM, Xu Y, Cheng Y-CN, Reichenbach JR (2004) Susceptibility weighted imaging (SWI). Magn Reson Med 52:612–618. doi: 10.1002/mrm.20198

Haase A, Frahm J, Matthaei D, et al (1986) FLASH imaging. Rapid NMR imaging using low flip-

angle pulses. J Magn Reson 67:258–266. doi: 10.1016/0022-2364(86)90433-6
Keuken MC, Bazin P-L, Crown L, et al (2014) Quantifying inter-individual anatomical variability in the subcortex using 7 T structural MRI. Neuroimage 94:40–46. doi: 10.1016/j.neuroimage.2014.03.032
Kramer AF, Erickson KI, Colcombe SJ (2006) Exercise, cognition, and the aging brain. J Appl Physiol 101:1237–1242. doi: 10.1152/japplphysiol.00500.2006
Langkammer C, Schweser F, Krebs N, et al (2012) Quantitative susceptibility mapping (QSM) as a means to measure brain iron? A post mortem validation study. Neuroimage 62:1593–1599. doi: 10.1016/J.NEUROIMAGE.2012.05.049
Logothetis NK, Wandell BA (2004) Interpreting the BOLD Signal. Annu Rev Physiol 66:735–769. doi: 10.1146/annurev.physiol.66.082602.092845
Marques JP, Kober T, Krueger G, et al (2010) MP2RAGE, a self bias-field corrected sequence for improved segmentation and T1-mapping at high field. Neuroimage 49:1271–1281. doi: 10.1016/J.NEUROIMAGE.2009.10.002
O'Reilly TPA, Webb AG, Brink WM (2016) Practical improvements in the design of high permittivity pads for dielectric shimming in neuroimaging at 7 T. J Magn Reson 270:108–114. doi: 10.1016/j.jmr.2016.07.003
Parkes LM, Schwarzbach J V., Bouts AA, et al (2005) Quantifying the spatial resolution of the gradient echo and spin echo BOLD response at 3 Tesla. Magn Reson Med 54:1465–1472. doi: 10.1002/mrm.20712
Pathak AP, Kim E, Zhang J, Jones M V. (2011) Three-Dimensional imaging of the mouse neurovasculature with magnetic resonance microscopy. PLoS One 6:. doi: 10.1371/journal.pone.0022643
Peters R (2006) Ageing and the brain. Postgrad Med J 82:84–8. doi: 10.1136/pgmj.2005.036665
Pfeifer RA (1927) Die Angioarchitektonik der Großhirnrinde. Eur Neurol 65:166–173. doi: 10.1159/000166076
Pfeifer RA (1940) Die angioarchitektonische areale Gliederung der Grosshirnrinde auf Grund vollkommener Gefa□ssinjektionspra□parate vom Gehirn des Macacus rhesus anatomisch dargestellt. G. Thieme
Seiyama A, Seki J, Tanabe HC, et al (2004) Circulatory basis of fMRI signals: relationship between changes in the hemodynamic parameters and BOLD signal intensity. Neuroimage 21:1204–14. doi: 10.1016/j.neuroimage.2003.12.002
Serres B, Deistung A, Schäfer A, et al (2015) Automatic Segmentation of the Venous Vessel Network Based on Quantitative Susceptibility Maps and its Application to Investigate Blood Oxygenation. Proc Intl Soc Mag Reson Med 23:0169
Shaaban CE, Aizenstein HJ, Jorgensen DR, et al (2017) In Vivo Imaging of Venous Side Cerebral Small-Vessel Disease in Older Adults: An MRI Method at 7T. AJNR Am J Neuroradiol 38:1923–1928. doi: 10.3174/ajnr.A5327
Stüber C, Morawski M, Schäfer A, et al (2014) Myelin and iron concentration in the human brain: A quantitative study of MRI contrast. Neuroimage 93:95–106. doi: 10.1016/J.NEUROIMAGE.2014.02.026
Turner R (2002) How much codex can a vein drain? Downstream dilution of activation-related cerebral blood oxygenation changes. Neuroimage 16:1062–1067. doi: 10.1006/nimg.2002.1082
Voss MW, Nagamatsu LS, Liu-Ambrose T, Kramer AF (2011) Exercise, brain, and cognition across the life span. J Appl Physiol 111:1505–13. doi: 10.1152/japplphysiol.00210.2011
Wahlund LO, Barkhof F, Fazekas F, et al (2001) A new rating scale for age-related white matter changes applicable to MRI and CT. Stroke 32:1318–22
Wang Y, Liu T (2015) Quantitative susceptibility mapping (QSM): Decoding MRI data for a tissue magnetic biomarker. Magn Reson Med 73:82–101. doi: 10.1002/mrm.25358
Ward PGD, Ferris NJ, Raniga P, et al (2018) Combining images and anatomical knowledge to improve automated vein segmentation in MRI. Neuroimage 165:294–305. doi: 10.1016/j.neuroimage.2017.10.049
Wayne Martin WR, Ye FQ, Allen PS (1998) Increasing striatal iron content associated with normal aging. Mov Disord 13:281–286. doi: 10.1002/mds.870130214
Woerz S, Rohr K (2004) A New 3D Parametric Intensity Model for Accurate Segmentation and

Quantification of Human Vessels. In: Proceedings of MICCAI. pp 491–499
Zecca L, Stroppolo A, Gatti A, et al (2004) The role of iron and copper molecules in the neuronal vulnerability of locus coeruleus and substantia nigra during aging